The Astrophysical Journal, 925:58 (13pp), 2022 January 20 https://doi.org/10.3847/1538-4357/ac3981

Inferring Kilonova Population Properties with a Hierarchical Bayesian Framework. I. Nondetection Methodology and Single-event Analyses

Siddharth R. Mohite[1,2,15], Priyadarshini Rajkumar[3], Shreya Anand[4], David L. Kaplan[1], Michael W. Coughlin[5], Ana Sagués-Carracedo[6], Muhammed Saleem[5], Jolien Creighton[1], Patrick R. Brady[1], Tomás Ahumada[7], Mouza Almualla[8], Igor Andreoni[4], Mattia Bulla[9], Matthew J. Graham[4], Mansi M. Kasliwal[4], Stephen Kaye[10], Russ R. Laher[11], Kyung Min Shin[12], David L. Shupe[11], and Leo P. Singer[13,14]

[1] Center for Gravitation, Cosmology and Astrophysics, Department of Physics, University of Wisconsin–Milwaukee, P.O. Box 413, Milwaukee, WI 53201, USA srmohite@uwm.edu
[2] Center for Computational Astrophysics, Flatiron Institute, 162 5th Ave, New York, NY 10010, USA
[3] Department of Physics and Astronomy, Texas Tech University, Lubbock, TX 79409-1051, USA
[4] Division of Physics, Mathematics and Astronomy, California Institute of Technology, Pasadena, CA 91125, USA
[5] School of Physics and Astronomy, University of Minnesota, Minneapolis, Min 55455, USA
[6] The Oskar Klein Centre, Department of Physics, Stockholm University, AlbaNova, SE-106 91 Stockholm, Sweden
[7] Department of Astronomy, University of Maryland, College Park, MD 20742, USA
[8] Department of Physics, American University of Sharjah, PO Box 26666, Sharjah, UAE
[9] The Oskar Klein Centre, Department of Astronomy, Stockholm University, AlbaNova, SE-10691 Stockholm, Sweden
[10] Caltech Optical Observatories, California Institute of Technology, Pasadena, CA 91125, USA
[11] IPAC, California Institute of Technology, 1200 E. California Blvd, Pasadena, CA 91125, USA
[12] California Institute of Technology, Pasadena, CA 91125, USA
[13] Astrophysics Science Division, NASA Goddard Space Flight Center, MC 661, Greenbelt, MD 20771, USA
[14] Joint Space-Science Institute, University of Maryland, College Park, MD 20742, USA
Received 2021 July 15; revised 2021 November 5; accepted 2021 November 12; published 2022 January 25

Abstract

We present `nimbus`: a hierarchical Bayesian framework to infer the intrinsic luminosity parameters of kilonovae (KNe) associated with gravitational-wave (GW) events, based purely on nondetections. This framework makes use of GW 3D distance information and electromagnetic upper limits from multiple surveys for multiple events and self-consistently accounts for the finite sky coverage and probability of astrophysical origin. The framework is agnostic to the brightness evolution assumed and can account for multiple electromagnetic passbands simultaneously. Our analyses highlight the importance of accounting for model selection effects, especially in the context of nondetections. We show our methodology using a simple, two-parameter linear brightness model, taking the follow-up of GW190425 with the Zwicky Transient Facility as a single-event test case for two different prior choices of model parameters: (i) uniform/uninformative priors and (ii) astrophysical priors based on surrogate models of Monte Carlo radiative-transfer simulations of KNe. We present results under the assumption that the KN is within the searched region to demonstrate functionality and the importance of prior choice. Our results show consistency with `simsurvey`—an astronomical survey simulation tool used previously in the literature to constrain the population of KNe. While our results based on uniform priors strongly constrain the parameter space, those based on astrophysical priors are largely uninformative, highlighting the need for deeper constraints. Future studies with multiple events having electromagnetic follow-up from multiple surveys should make it possible to constrain the KN population further.

Unified Astronomy Thesaurus concepts: Bayesian statistics (1900); Hierarchical models (1925); Neutron stars (1108); Gravitational wave sources (677); Surveys (1671); Compact objects (288)

1. Introduction

Mergers of neutron stars and neutron-star–black hole binaries (BNS and NSBH) present unique opportunities to probe multimessenger astrophysics (e.g., Metzger 2019). While they are among the best sources of gravitational-wave (GW) emission detectable by GW observatories (Abbott et al. 2019, 2020) such as Advanced LIGO and Advanced Virgo (Aasi et al. 2015; Acernese et al. 2015), their potential detection in the electromagnetic (EM) spectrum by surveys around the world represents one of the most challenging searches for astrophysical transients. During the merger, significant amounts of neutron-star (NS) matter are ejected at subrelativistic speeds due to either tidal or hydrodynamical forces; the radioactive decay of *r*-process elements synthesized in the neutron-rich merger ejecta powers a thermal ultraviolet, optical, and near-infrared transient, often referred to as a kilonova (KN) (Li & Paczyński 1998; Rosswog 2005; Metzger et al. 2010; Tanaka & Hotokezaka 2013). Despite their color and luminosity evolution being viewing-angle dependent (Kasen et al. 2015; Bulla 2019; Kawaguchi et al. 2020; Korobkin et al. 2021; Zhu et al. 2021b), their (largely) isotropic emission makes KNe one of the promising targets for EM counterpart follow-up observations (Roberts et al. 2011). However, they can be short lived, faint, and peak in the infrared, making detection difficult (Kasen et al. 2015; Barnes et al. 2016; Tanaka 2016; Metzger 2019; Nakar 2020).

[15] LSSTC Data Science Fellow.

From an observational standpoint, the GW detection of the BNS merger GW170817 (Abbott et al. 2017a) provided the first, and only, multimessenger follow-up of a GW event to yield an associated KN (AT2017gfo) to date (Abbott et al. 2017b). Observations were recorded in the ultraviolet, optical, and near-infrared (Andreoni et al. 2017; Chornock et al. 2017; Coulter et al. 2017; Cowperthwaite et al. 2017; Drout et al. 2017; Evans et al. 2017; Kasliwal et al. 2017, 2022; Kilpatrick et al. 2017; Lipunov et al. 2017; McCully et al. 2017; Nicholl et al. 2017; Shappee et al. 2017; Soares-Santos et al. 2017; Pian et al. 2017; Smartt et al. 2017; Tanvir et al. 2017; Utsumi et al. 2017). These observations have highlighted the ability to test models of KNe and provide constraints on the ejecta mass and velocity (Abbott et al. 2017c; Cowperthwaite et al. 2017; Perego et al. 2017; Pian et al. 2017; Smartt et al. 2017; Tanaka et al. 2017; Waxman et al. 2018; Coughlin et al. 2019a; Kawaguchi et al. 2020; Heinzel et al. 2021; Raaijmakers et al. 2021), *r*-process elemental abundances (Côté et al. 2018; Hotokezaka et al. 2018; Radice et al. 2018; Tanaka et al. 2018; Siegel 2019; Hotokezaka & Nakar 2020), the NS equation of state (Foucart et al. 2018; Coughlin et al. 2018a; Radice & Dai 2019; Hinderer et al. 2019; Breschi et al. 2021; Nicholl et al. 2021), and the Hubble constant (Hotokezaka et al. 2019; Dietrich et al. 2020; Dhawan et al. 2020).

There are a plethora of studies in the literature that model the luminosity evolution of KNe (Kasen et al. 2017; Coughlin et al. 2018a; Wollaeger et al. 2018; Bulla 2019; Kawaguchi et al. 2020; also see references in Metzger 2019). Despite the detection of the KN from GW170817, there are significant uncertainties in the model parameter space (Barnes et al. 2016; Rosswog et al. 2017; Zhu et al. 2018; Kasliwal et al. 2022; Wu et al. 2019; Heinzel et al. 2021). These uncertainties primarily stem from the range of ejecta masses expected from such mergers and the content of nuclear matter assumed in the models (Barnes et al. 2021; Foucart et al. 2021; Just et al. 2022; Kullmann et al. 2022). While uncertainties in the mass ejected from BNS systems have been shown to be driven mostly by the total mass and mass ratio of the system (Bauswein et al. 2013; Hotokezaka et al. 2013; Köppel et al. 2019; Kiuchi et al. 2019), those in models for NSBH systems are influenced by the mass ratio, BH spin, and NS radius (Etienne et al. 2009; Kyutoku et al. 2015; Kawaguchi et al. 2016; Foucart et al. 2018; Zhu et al. 2021a).

The third observing run of Advanced LIGO and Virgo (O3),[16] which lasted 11 months, yielded a total of 15 publicly announced NSBH and BNS candidates. Several teams, including the Global Relay of Observatories Watching Transients Happen (GROWTH; Kasliwal et al. 2020), Electromagnetic counterparts of GW sources at the Very Large Telescope (ENGRAVE; Levan 2020), Global Rapid Advanced Network Devoted to the Multi-messenger Addicts (GRANDMA; Antier et al. 2020), Gravitational-wave Optical Transient Observer (GOTO; Gompertz et al. 2020), All Sky Automated Survey for SuperNovae (ASAS-SN; de Jaeger et al. 2022), Asteroid Terrestrial Last Alert System (ATLAS; Tonry et al. 2018), Panoramic Survey Telescope and Rapid Response System (Pan-STARRS; Chambers et al. 2016), MASTER-Net (Lipunov et al. 2017), Dark Energy Survey Gravitational Wave Collaboration (DES-GW; Soares-Santos et al. 2017), and Japanese collaboration for Gravitational wave ElectroMagnetic follow-up (J-GEM; Sasada et al. 2021) conducted wide-field searches within the sky maps of BNS and NSBH candidates and pursued follow-up of interesting transient candidates found therein, but no plausible EM counterparts were found (e.g., Coughlin et al. 2019b).

Nevertheless, the apparent dearth of counterparts during all of O3 can illuminate our understanding of the intrinsic properties of KNe. On an individual GW event basis, observational upper limits can be used to constrain the KN emission from a potentially associated counterpart and infer properties of the binary (Hosseinzadeh et al. 2019; Andreoni et al. 2020; Anand et al. 2020; Morgan et al. 2020). Other works, e.g., Coughlin et al. (2019b), Lundquist et al. (2019a), Gompertz et al. (2020), Antier et al. (2020), and Kasliwal et al. (2020), have demonstrated ways to synthesize survey observations for a suite of GW events to constrain the KN population as a whole. In particular, Kasliwal et al. (2020) formulated a method for constraining the luminosity function of the KN population. Assuming a non-uniform distribution of KN initial luminosities between -10 and -20 absolute magnitude, their findings suggest that no more than 57% (89%) of KNe could be brighter than -16.6 mag assuming a flat (fading at 1 mag day^{-1}) evolution (Kasliwal et al. 2020).

In this paper, we present `nimbus` (Mohite 2021), a hierarchical Bayesian framework to infer the intrinsic luminosity parameters of the population of KNe associated with GW events, based purely on nondetections. Key features of this framework include the simultaneous use of probabilistic source distance information from GW observations and corresponding upper limits from EM surveys, accounting for the fraction of the sky map searched by a given survey for each event, self-consistent inclusion of the probability of a GW event being of astrophysical origin ($p_{\rm astro}$) and the ability to model multiband luminosity evolution. The framework is agnostic to the specific luminosity model used and thus can be used to constrain a wide variety of models in the literature.

As a first example and proof of concept, we demonstrate realistic constraints possible on the KN emission from the past follow-up of the event GW190425 (Abbott et al. 2020) conducted with the Zwicky Transient Facility (ZTF) (Coughlin et al. 2019c). ZTF is an optical time-domain survey, consisting of a CCD camera with a 47 deg^2 field of view installed on the 48 inch Samuel Oschin Schmidt Telescope at the Palomar Observatory. Scanning the sky at an areal survey speed of $\sim$3750 deg^2 per hour in three custom filters, ZTF-*g*, ZTF-*r*, and ZTF-*i*; it reaches a median depth of 20.4 mag in 30 s exposures in its nominal nightly survey but can also conduct deeper target-of-opportunity follow-up of external events (Coughlin et al. 2019d); for a comprehensive review of the ZTF instrument, software, and survey, see Bellm et al. (2019), Masci et al. (2019), Graham et al. (2019), Dekany et al. (2020).

Among the 13 events searched by ZTF in Advanced LIGO's third observing run (Kasliwal et al. 2020) that could have a probable EM counterpart, based on the probability of the system containing an NS, i.e., p(BNS) or p(NSBH), GW190425 is so far the only significant binary merger event confirmed by LIGO and Virgo (Abbott et al. 2020) to likely be a BNS based on the posterior inference of its masses; therefore, our analysis herein focuses on this event alone. GW190425 was located at a distance of 159^{+69}_{-71} Mpc and its final 90% credible localization spanned 8284 deg^2 (Abbott et al. 2020). For GW190425, ZTF observed $\sim$8000 deg^2, corresponding to

[16] https://gracedb.ligo.org/superevents/public/O3/

45% probability of the initial BAYESTAR sky map (Singer & Price 2016), which reduced to 21% integrated probability within the 90% credible region of the LALInference sky map (Veitch et al. 2015) and attained a median depth of $m_{\rm AB} \approx 21$ mag in the g and r bands (Coughlin et al. 2019d). For the purpose of this analysis, we consider ZTF areal coverage within the entire LALInference sky map, which corresponds to 32% probability. No KN was identified in the observed region of this event by ZTF or other optical telescopes (Lipunov et al. 2019; Lundquist et al. 2019b; De et al. 2019; Xu et al. 2019; Kasliwal et al. 2019; McBrien et al. 2019; Smith et al. 2019; Steeghs et al. 2019; Blazek et al. 2019; Li et al. 2019), or for any other GW event followed up with ZTF (Kasliwal et al. 2020).

This paper is organized as follows. In Section 2, we provide a detailed description of the Bayesian framework including a derivation of the model posterior and important aspects that impact the inference. We then present our main inference results on GW190425 using two different prior assumptions in Section 3. We also use this section to compare our results with those obtained from `simsurvey` (Feindt et al. 2019), a simulation tool for astronomical surveys previously used in the literature to constrain KN luminosity distributions (Kasliwal et al. 2020). We then conclude with a discussion of our results and future outlook in Section 4.

2. Bayesian Framework

In order to derive constraints on KN parameters, we make use of a hierarchical Bayesian statistical framework. Our goal is to find the posterior probability distribution of the parameters of interest $\vec{\theta}$, given the data $\{d^i\}$. The derivation here follows analogous derivations of hierarchical population inference in GW literature (Farr et al. 2015; Gaebel et al. 2019; Mandel et al. 2019).

2.1. Model Definitions

For this paper, we model the luminosity evolution of KNe using a two-parameter, linear family of light curves (as adopted in Kasliwal et al. 2020). However, we will discuss extensions of our framework to other models as well. The absolute magnitude (M) in a given filter λ is given as a linear function of time (t),

$$M^{\lambda}(t) = M_0 + \alpha(t - t_0), \tag{1}$$

where t_0 is the initial time of the KN transient. We can see that the two parameters (M_0, α), which represent an initial absolute magnitude and evolution rate, respectively, completely define the evolution at all times. Therefore, for this simplistic parameterization, $\vec{\theta} = \{M_0, \alpha\}$. We emphasize that our motivation to implement such a simple model is to demonstrate the framework and due to the fact that we rely on follow-up observations of KNe up to 3 days following the merger time, where such models are a relatively good fit to the data (see Section 3.3 and Section 4).

Before we begin with our derivation, we will state our notation as follows:

1. N_E : Total number of events that were followed up, indexed by i.
2. N_F : Total number of fields of view for which EM observations have been recorded, indexed by f. For purposes of improved reference model subtraction, many optical/infrared surveys use discrete fields for observations rather than allowing complete freedom (Ghosh et al. 2017; Coughlin et al. 2018b and references therein). However, this can be generalized to any discretization of the sky such as HEALPIX (Hierarchical Equal Area isoLatitude Pixelization;[17] Górski et al. 2005) if needed.
3. N_f : Total number of observations for field f.
4. t_j^f : Time of observation, indexed by j for each field f over the duration of follow-up of the event. j would run over the total number of observations for each field (N_f).
5. t_0 : Initial time of the KN transient, which corresponds to the initial absolute magnitude M_0.
6. $\bar{f}$: Index for fields not including the field f.
7. $\bar{F}$: Hypothesis that the KN is not in any of the observed fields.
8. A : Hypothesis that the event is of astrophysical origin.
9. T : Hypothesis that the event is of terrestrial origin (implying that the event is spurious).
10. $P^i(A)$, : The probability of the $i^{\rm th}$ event being of astrophysical (A) origin. This is an estimate provided by the LIGO–Virgo–KAGRA collaboration for the associated GW event. It can either be a low-latency estimate or an update provided after a refined analysis.
11. $\{d^i\}$: The set of EM data associated with all events, indexed by i. We will further index this data by the field index f and time of observation index j in our derivation below. For this study, we take our data to be the set of limiting (apparent) magnitudes $\{m_l^{i,f,j}\}$ in each field at the given time of observation.

2.2. Derivation of the Model Posterior

We begin our derivation of the model posterior with the basic equation of Bayes' law:

$$p(M_0, \alpha|\{d^i\}) = \frac{p(\{d^i\}|M_0, \alpha)p(M_0, \alpha)}{p(\{d^i\})}, \tag{2}$$

where $p(\{d^i\}|M_0, \alpha)$ is the likelihood, $p(M_0, \alpha)$ is the prior distribution of the parameters M_0 and α, and $p(\{d^i\})$ is the evidence. We carry out analyses based on different prior assumptions and show the effect it has on the posterior distribution of the KN parameters in Section 3. The likelihood represents the probability density of observing the data d^i given a model, for a set of events indexed by i, while the evidence is the probability of observing the data, marginalized over all parameters and serves as a normalization factor in the inference. Further, each event and its associated data are assumed to be independent. The likelihood $p(\{d^i\}|M_0, \alpha)$ can then be written as a product over events:

$$p(\{d^i\}|M_0, \alpha) = \prod_{i=1}^{N_E} [p(d^i|M_0, \alpha)]. \tag{3}$$

There are two possibilities for any given event—either the event is astrophysical (A) or it is non-astrophysical/terrestrial (T). We note that the probability of the latter hypothesis is $(1 - P^i(A))$. We thus split the likelihood into two terms using

[17] https://healpix.sourceforge.io/

the relative probabilities of each hypothesis,

$$p(\{d^i\}|M_0,\,\alpha) = \prod_{i=1}^{N_E}[p(d^i|M_0,\,\alpha,\,A)P^i(A) + p(d^i|T)(1-\boldsymbol{P^i(A)})]. \quad (4)$$

The assumption in the last term in the parentheses is that the contribution to the likelihood cannot depend on the parameters of the KN model if the event is of terrestrial origin. This is straightforward to check because in the case of a purely terrestrial event ($P^i(A) = 0$), we must recover the prior when performing inference.

We now use the fact that, for any event (indexed by i), EM observations are distributed over N_F fields (indexed by f) at times of observations (indexed by j) such that every observation has associated limiting magnitudes ($m_l^{i,f,j}$). As stated above, we take our data d^i for each event to be the set of these observed limiting (apparent) magnitudes $\{m_l^{i,f,j}\}$, i.e., $d^i \equiv \{m_l^{i,f,j}\}$. The likelihood thus becomes,

$$p(\{d^i\}|M_0,\,\alpha) = \prod_{i=1}^{N_E}[p(\{m_l^{i,f,j}\}|M_0,\,\alpha,\,A)P^i(A) + p(\{m_l^{i,f,j}\}|T)(1-\boldsymbol{P^i(A)})]. \quad (5)$$

Furthermore, under the astrophysical hypothesis (A), the likelihood can be split into two more terms given that there are two possibilities for the KN event—

1. The KN is located within an observed field f and, consequently, not in any of the other fields ($\bar{f}$). In this case, we need to find the probability that the KN is within a field f, i.e., $P(f)$, and sum the contributions to the likelihood from each field. The overall likelihood contribution from this hypothesis is

$$\sum_{f=1}^{N_F}(p(\{m_l^{i,f}\}|M_0,\,\alpha,\,A,\,f) \times \prod_{\bar{f}} p(\{m_l^{i,\bar{f}}\}|A,\,f)P(f)).$$

2. The KN event is not located in any observed field (hypothesis $\bar{F}$). This case has a probability equal to $(1-\sum_{f=1}^{N_F}P(f))$. The overall likelihood contribution from this hypothesis is

$$\prod_f p(\{m_l^{i,f}\}|A,\,\bar{F})\left(1-\sum_{f=1}^{N_F}P(f)\right).$$

When information about a GW candidate event is released, it contains the 3D sky probability distribution of the location of the event, which includes the luminosity distance (d_L) to the source (Singer et al. 2016a, 2016b). Using this, it is straightforward to compute the probability for a KN to be present in a given field. Referring to Equation (3) in Singer et al. (2016a), the sum of probabilities over the sky is

$$P(f) = \sum_{k=0}^{N_{pix}^f}\rho_k, \quad (6)$$

where the sum is over the $N_{\rm pix}^f$ pixels that are contained within the field f and ρ_k is the probability of the event being in pixel k. The likelihood, written in terms of the hypothesis contributions stated above, then becomes

$$p(\{d^i\}|M_0,\,\alpha) = \prod_{i=1}^{N_E}\Big[\Big(\sum_{f=1}^{N_F}(p(\{m_l^{i,f}\}|M_0,\,\alpha,\,A,\,f) \prod_{\bar{f}} p(\{m_l^{i,\bar{f}}\}|A,\,f)P(f) + \prod_f p(\{m_l^{i,f}\}|A,\,\bar{F})\Big(1-\sum_{f=1}^{N_F}P(f)\Big)\Big)P^i(A) + \prod_f p(\{m_l^{i,f}\}|T)(1-\boldsymbol{P^i(A)})], \quad (7)$$

where the second and third terms in the parentheses correspond to the hypotheses that the KN position is outside all the observed fields and that the event is terrestrial in nature, respectively.

Because the observations in each field will have observation times associated with them, each field observation would constrain the model independently. Thus, the likelihood term for each field can be written as a product over the number of observations corresponding to that field:

$$p(\{d^i\}|M_0,\,\alpha) = \prod_{i=1}^{N_E}\Big[\Big(\sum_{f=1}^{N_F}(\prod_{j=1}^{N_f}p(m_l^{i,f,j}|M_0,\,\alpha,\,A,\,f) \prod_{\substack{\bar{f}=1,\\ \bar{f}\neq f}}^{N_F}p(m_l^{i,\bar{f}}|A,\,f)P(f)) + \prod_f p(m_l^{i,f}|A,\,\bar{F})\Big(1-\sum_{f=1}^{N_F}P(f)\Big)\Big)P^i(A) + \prod_f p(m_l^{i,f}|T)(1-\boldsymbol{P^i(A)})]. \quad (8)$$

We now focus on the first term in the likelihood for each field $p(m_l^{i,f,j}|M_0,\,\alpha,\,A,\,f)$. In order to simplify this term and derive an expression for the same, we note that, in reality, a telescope measures an apparent magnitude (m_j) instead of an absolute magnitude. One can rewrite this likelihood term, using conditional probability, as an integral over the apparent magnitude of the KN event:

$$p(m_l^{i,f,j}|M_0,\,\alpha,\,A,\,f) = \int_{-\infty}^{\infty} p(m_l^{i,f,j}|m_j)p(m_j|M_0,\,\alpha,\,A,\,f)dm_j. \quad (9)$$

The relationship between the apparent magnitude (m), absolute magnitude (M), and luminosity distance (d_L) of an astrophysical source is given as

$$m = M + 5\log_{10}\left(\frac{d_L}{10\text{pc}}\right) \quad (10)$$

or equivalently,

$$d_L = 10^{\left(\frac{m-M}{5}\right)}\left(\frac{1}{10^5}\right)\text{Mpc}. \quad (11)$$

The above formulae do not include the effects of extinction. We account for Milky Way extinction in our framework by appropriately modifying the limiting magnitudes for each field and filter. We make use of the `dustmaps` package (Green 2018) and its implementation of the Schegel–Finkbeiner–Davis (SFD) dust map (Schlafly & Finkbeiner 2011) to derive extinction values. Also, from Equation (11), we can derive a limiting distance $d_{\rm lim}^{i,f,j}$ for a corresponding limiting magnitude $m_l^{i,f,j}$. The intrinsic parameters of the KN (M_0, α) along with the observation time (t_j) uniquely determine the absolute magnitude ($M_j(M_0,\,\alpha)$) of the KN, at any given time.

Equation (11) shows that for such a given absolute magnitude M, the apparent magnitude and distance are dependent variables that uniquely define each other. It is possible to relate the apparent magnitude distribution ($p(m_j|M_0, \alpha, A, f)$) in the integral above to the marginal distance distribution ($p_f(d_L)$) for each field f, which can be derived from the GW sky map, as

$$p(m_j|M_0, \alpha, A, f) = p_f(d_L)\frac{d\ d_L}{dm_j}(M_0, \alpha). \tag{12}$$

We can thus rewrite the integral in Equation (9) as

$$\begin{aligned} &p(m_l^{i,f,j}|M_0, \alpha, A, f) \\ &= \int_0^\infty p(m_l^{i,f,j}|m_j(d_L, M_0, \alpha))p_f(d_L)d\ d_L. \end{aligned} \tag{13}$$

Because this is a nondetection study, the only viable limiting magnitudes for nondetection are those that are strictly shallower (brighter) than the apparent magnitude from the KN model. We implement this by using a uniform distribution function for the conditional density $p(m_l^{i,f,j}|m_j(d, M_0, \alpha))$ as

$$p(m_l^{i,f,j}|m_j(d_L, M_0, \alpha)) \propto \begin{cases} \dfrac{1}{(m_j - m_l^{i,f,j})}; m_j \leqslant m_l^{\rm high} \\ \dfrac{1}{(m_l^{\rm high} - m_l^{\rm low})}; m_j > m_l^{\rm high} \end{cases}, \tag{14}$$

where $m_l^{\rm low}$, $m_l^{\rm high}$ are the lower and upper limits of the range of limiting magnitudes from the survey or distance information, respectively. See Section 2.3 for a more detailed discussion on the choice of these limits. Further, it is important to account for the probabilistic nature of each limiting magnitude when considering the likelihood of any given model. We incorporate this requirement into our likelihood with a logistic function $\Phi(d_L - d_{\rm lim}^{i,f,j})$. The logistic function ensures a smooth turnover in the likelihood between distances (apparent magnitudes) that pass the limiting distance (limiting magnitude) constraints and those that do not. From Equation (11), we can write the logistic function in terms of the distance as

$$\Phi(d_L - d_{\rm lim}^{i,f,j}) = \frac{1}{1 + e^{-a(d_L - d_{\rm lim}^{i,f,j} + b)}}. \tag{15}$$

We choose the constants a and b in Equation (15) based on errors in the limiting magnitude such that a 3σ error in $m_l^{i,f,j}$ corresponds to the distance at which the logistic function in Equation (15) is set to the cumulative probability weight of a Gaussian distribution beyond the lower 2σ limit ($\sim$2.3%). Combining Equations (14) and (15), the likelihood term in Equation (13) can be evaluated up to a normalization constant k.

Because the total likelihood in Equation (8) is a sum of probability densities, care must be taken to normalize each term, corresponding to each hypothesis, separately. The constant k can be derived by normalizing the likelihood term in Equation (13) between the appropriate limiting magnitude limits, or more directly between appropriate limiting distance limits:

$$k = \frac{1}{\int_{m_l^{\rm low}}^{m_l^{\rm high}} p(m_l^{i,f,j}|M_0, \alpha, A, f)dm_l^{i,f,j}}. \tag{16}$$

These limits can be chosen based on the extent of the marginal distance distribution for each field. We provide specific details of our assumptions for these limits in Section 3.

This normalization also ensures that we account for selection effects based on the limiting magnitude limits of the survey. We defer the discussion of the impact this has on the inference to Section 2.3. The remaining terms in the field (f), non-field ($\bar{f}$), and terrestrial (T) hypotheses from Equation (8) must be normalized. We assume that each of these terms follows a uniform distribution between the survey limits $m_l^{\rm low}$–$m_l^{\rm high}$. This assumption largely simplifies the form of the likelihood. While it is not necessary to assume such a form for each of these terms, and one can construct more complex distributions based on realistic data, this choice does not impact the inference because these distributions must necessarily be independent of the model parameters. This gives us a normalized density of

$$\begin{aligned} p(m_l^{i,\bar{f}}|A, f) &= p(m_l^{i,f}|A, \bar{F}) = p(m_l^{i,f}|T) \\ &= \frac{1}{(m_l^{\rm high} - m_l^{\rm low})}. \end{aligned} \tag{17}$$

This simplifies the likelihood in Equation (8) to give us a posterior

$$\begin{aligned} p(M_0, \alpha|\{d^i\}) \propto \prod_{i=1}^{N_E} \Bigg[&\left(\sum_{f=1}^{N_F} \left(\frac{\prod_j p(m_l^{i,f,j}|M_0, \alpha, A, f)}{\prod_j p(m_l^{i,f,j}|A, \bar{f})} \right) P(f) \right) \\ &+ \left(1 - \sum_{f=1}^{N_F} P(f)\right) \Bigg) P^i(A) \\ &+ (1 - \boldsymbol{P^i(A)}) \Bigg] p(M_0, \alpha). \end{aligned} \tag{18}$$

2.3. Impact of Using Survey Limits and Distance Limits on Inference

We derived our model posterior for the framework in Section 2.2. As seen in Equation (16), an important quantity to compute for the posterior is the normalization factor k, which depends on the choice of upper limits $m_l^{\rm low}$ and $m_l^{\rm high}$ and model parameters (M_0, α). Such a factor is akin to accounting for selection effects (see Mandel et al. 2019) where one has to normalize the likelihood of observing a given model (M_0, α) by the range of data supported by the model. From Equation (11), it is possible to express upper limits for a model equivalently in terms of the apparent magnitude or the distance. Thus, a range in one of the quantities directly specifies a range in the other. The choice of which quantity to use to calculate $m_l^{\rm low}$ and $m_l^{\rm high}$ significantly affects the result of the inference. There are two ways to select specific values for these normalizing parameters:

1. Survey limits: A straightforward method is to choose $m_l^{\rm low}$ and $m_l^{\rm high}$ directly from survey data when the telescope is observing. From Equation (11), this directly impacts the range of distances permitted for a given model (M_0, α) and gives a different normalization value for each model. Such a method ensures that the normalization realistically accounts for model biases in the case of nondetection.
2. Distance limits: Alternatively, we can choose to use the distance posterior from the GW sky-map data as our

source of ground truth such that we calculate $m_l^{\rm low}$ and $m_l^{\rm high}$ based on the full range of possible distances[18]. This will change the values of $m_l^{\rm low}$ and $m_l^{\rm high}$ for each model. However, as the range in distance is the same for each model, this ensures that the normalization factor is the same.

We note that our preferred results in this paper are those that use realistic survey upper limits. Unless stated otherwise, our reference to results in general will be with this choice. We present the differences that result from these two choices in Section 3.1.

3. Kilonova Inference Using GW190425

GW190425 was a highly significant ($p_{\rm astro} \sim 0.999$; Abbott et al. 2020) GW event that was followed up by ZTF (Coughlin et al. 2019c) with an overall sky coverage of ~32% of the total sky map. Inferences on the component masses of the detected binary show it to be consistent with a BNS, although the possibility of either or both components being BHs cannot be ruled out from GW data alone. Here, we present results using the Bayesian framework `nimbus` described here with upper limits from the ZTF follow-up of GW190425 to derive posterior constraints on KN parameters of the model light curve for BNS mergers. We note that unlike the band-specific linear evolution shown in Equation (1), we adopt a single "average-band" linear model with parameters (M_0, α) for our analyses presented here. This "average-band" model effectively assumes the same color evolution in all bands, allowing us to use ZTF observations in all filters for our analysis. This simplified model is conducive for testing the `nimbus` framework as it significantly reduces the model parameter space (because KN models predict a wide diversity in expected color evolution). For example, using this linear model fit, GW170817 has $M_0 = -16.6$ mag and $\alpha = 1$ mag day^{-1} (Kasliwal et al. 2020). Our analyses rely on two different prior distribution choices for (M_0, α): (i) uniform or agnostic priors (explained in Section 3.1) and (ii) astrophysical priors motivated from theory and numerical modeling (explained in Section 3.3). We limit our analyses to use follow-up data up to 3 days from the trigger time because realistic models predict that most KNe will fade beyond the median ZTF limiting magnitude of 21 $m_{\rm AB}$ (for this event) within 72 hr after the trigger time (see Section 4).

In order to limit the effects of Milky Way extinction in the fields surveyed, we place a conservative threshold by excluding fields that have $E(B-V) > 2$ mag. For the remainder of the paper, we make a simplifying assumption that the KN associated with GW190425 is located within the searched region.[19] We ran simulations taking the full GW190425 sky map into account and found the results to be largely unconstraining; hence we adopt the above assumption in order to demonstrate the constraints possible with `nimbus` in an ideal sky coverage scenario. Our constraints on KN model parameters, obtained using both prior choices stated above, are displayed in Table 1. In order to derive our constraints and plot our posterior probabilities in this paper, we make use of an interpolating or smoothing function such as the Gaussian Process module from `scikit-learn` (Pedregosa et al. 2011) to interpolate between our original samples from priors. We have checked that uncertainties from these interpolations (see Figure 2) are within the statistical variations of the observed limiting magnitudes across the ZTF quadrants for each field of observation, where these variations are $\geq$0.1 mag for a majority of fields. Section 3.1 with uniform priors demonstrates the functionality of the framework. In particular, our results in this section show the posterior constraints that are possible using the framework. In addition, we show how a general inference is sensitive to variations in sky coverage and $p_{\rm astro}$. We also use this section to illustrate the differences in results based on the two different normalization choices as explained in Section 2.3: choosing the faint and bright apparent magnitude limits based on the observed range from ZTF (Survey Limits) or based on the minimum and maximum distances from the GW distance posterior (Distance Limits). Section 3.3 demonstrates the ability to test astrophysical priors within the `nimbus` framework.

Table 1
90% Upper Limit of the Kilonova Initial Absolute Magnitude (M_0) for the Different Prior Choices in Section 3

Prior Choice	$M_0^{90\%}$ (mag)
Uniform-mlim	−16.63
Uniform-distance	−15.01
Astrophysical	−17.08

3.1. Uniform Priors

We first implement the framework assuming uniform priors for our model parameters $M_0 \sim \mathcal{U}(-20, -10)$mag , $\alpha \sim \mathcal{U}(-1, 2)$mag day^{-1}. According to our convention (see Equation (1)) a negative evolution rate would imply a rising light curve for the KN while a positive one would be decaying. While $\alpha < 0$ appears implausible based on our BNS KN model fits (see Section 3.3), KNe from NSBH systems can exhibit a slow rise (Anand et al. 2020) that could take $\gtrsim$2 days to peak. Within our time window of observations of 3 days, an NSBH KN model may be better approximated by a rising linear model than a fading one. Thus, we adopt a broad range for our evolution rate prior to accommodate rising to rapidly decaying KN models. Our prior on the initial magnitude is similarly broad, spanning a large fraction of the known transient phase space (Kasliwal 2011). Such a prior is uninformative with respect to the realistic emission models of KNe that have implications for how (M_0, α) could be distributed. The posterior densities we obtain via the framework are shown in the left panel of Figure 1. Broadly, we see that, as expected for a nondetection, there is more posterior support for dimmer models (larger values of M_0 and α) than brighter ones (smaller values of M_0 and α). Another expected trend is the increase of support for brighter M_0 values with respect to the evolution rate as we vary α from ~ -1 to 1 mag day^{-1}. A significant part of the parameter space that belongs to bright and rising models ($M_0 \lesssim -18$ and $\alpha \lesssim 0$) is disfavored over the rest of the models by factors of ~10–100. For most of the parameter space, where $M_0 \gtrsim -15$, our results cannot place any constraints.

The right panel of Figure 1 also compares the posterior constraints we obtain with two different normalization choices as explained in Section 2.3. The inference derived using realistic survey limits (`mlim-survey`; green contours) relies on the range of limiting magnitudes obtained from ZTF during

[18] Computationally, we bound the distance between a realistic lower limit and the upper 5σ value from the distance posterior.

[19] `nimbus` has the capability to accommodate the excluded part of the sky map (see Figure 2).

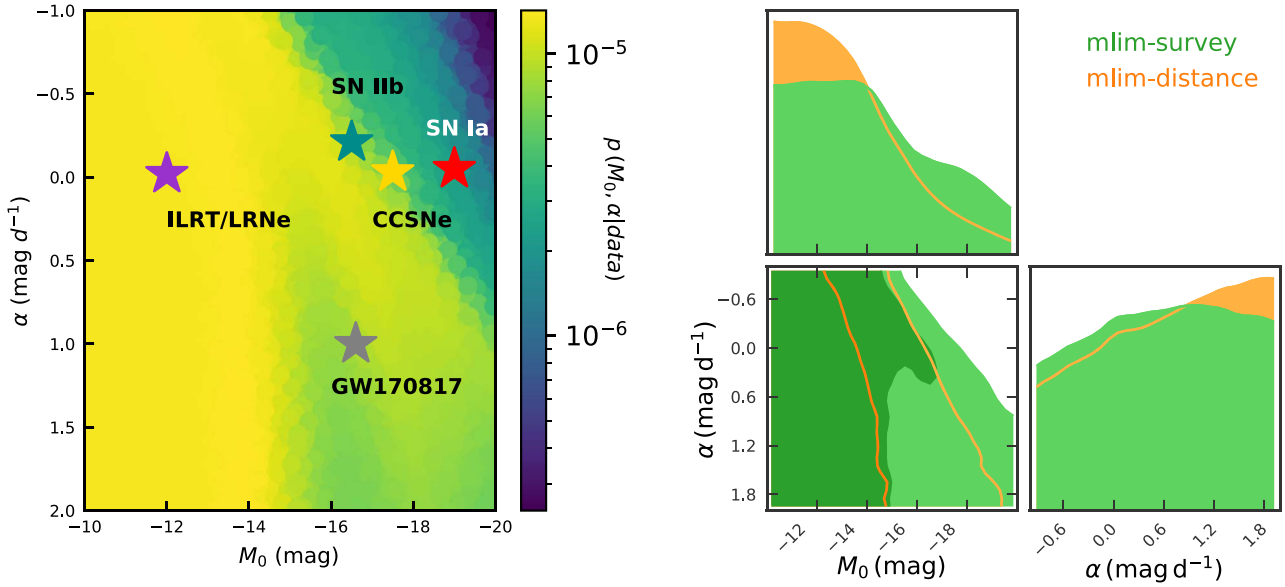

Figure 1. (Left) 2D posterior probability plot of KN model parameters (initial absolute magnitude M_0, evolution rate α) with uniform priors, $M_0 \sim \mathcal{U}(-20, -10)$mag, $\alpha \sim \mathcal{U}(-1, 2)$mag day^{-1}, and normalization over realistic survey limits. Representative points are shown for the characteristic peak magnitude and rise rate (derived from the characteristic timescale) for some categories of transients (Kasliwal 2011; C. Fremling et al., in preparation)—Type Ia supernova (SN Ia; red), core collapse SNe (CCSNe; gold), faint, fast SN IIb (dark-cyan), Intermediate Luminosity Red Transient/Luminous Red Novae (ILRT/LRNe; dark-orchid), and GW170817 (gray). (Right) Corner plot showing the 2D and corresponding 1D marginalized posterior distributions of the KN model parameters for the two different normalization schemes detailed in Section 2.3—using realistic survey limits from ZTF data for GW190425, which are between 15 and 23 mag (green; `mlim-survey`) and distance limits obtained for each model drawn using 5σ distance limits obtained from the sky-map distance posterior for each field (orange; `mlim-distance`). Contours indicate 68% and 95% confidence regions. Nonmonotonic features in both panels (e.g., 68% green contour in the right panel) indicate the effects of model normalization. Details in Sections 2.3 and 3.1.

the follow-up of GW190425. For this event, this corresponds to range limits of ($m_{\rm low} \approx 15$, $m_{\rm high} \approx 23$). On the other hand, posteriors obtained using distance limits (`mlim-distance`; orange contours) rely on the entire range of posterior distances from the 3D sky map for the event. While constraints from the two choices are quite similar with respect to the evolution rate, the `mlim-survey` method provides more support to models on the brighter end of the M_0 distribution compared to the `mlim-distance` method. This is understandable because having a restricted range of limiting magnitudes from the survey reduces the range of viable distances for brighter models, thereby providing a smaller parameter space that satisfies the likelihood. Accounting for this fact in the likelihood as a selection effect leads to an up-weighting of these brighter models with respect to the `mlim-distance` method. This is also the reason we see nonmonotonic features in the 2D posterior distributions with the `mlim-survey` method in both panels of Figure 1. The effects of normalization arise the most for models that are at the marginal boundary with respect to the upper limits. As mentioned previously, our preferred results in this paper are those that use the `mlim-survey` method.

As seen from Table 1, the 90% upper limit with a uniform prior is about $M_0^{90\%} = -16.63$ mag. We compare the result derived here to the probability of zero detections as a function of the absolute magnitude shown in Figure 9 of Kasliwal et al. (2020), which indicates a $\sim$7% probability for models with a similar initial absolute magnitude. Although the two separate constraints are consistent, there are significant differences between the two formalisms overall. The first is that our analysis assumes that an associated KN fell within the observed region. If we relax this assumption and use the $\sim$32% sky coverage in total for this event by ZTF, our inference over the entire sky-map region does not yield any meaningful constraints, as expected.

The second difference is that in this work, we infer the properties of a KN associated with GW190425, while the main result of Kasliwal et al. (2020) places constraints on the luminosity function of the KN population as a whole. While strong constraints on the KN emission from a single GW event are possible with a combination of complete sky coverage and deep upper limits, analyzing KN population properties importantly relies on several events observed with decent sky coverage and depth. We note, however, that GW190425 likely contributes significantly to the constraints in Kasliwal et al. (2020) given its nearby distance and ZTF median depth ($m \approx 21$ mag).

The 90% limit stated above is also significant in that it represents the extrapolated peak magnitude of GW170817 with an average decay rate of 1 mag day^{-1} (Kasliwal et al. 2020). From the left panel in Figure 1, we can see that the data for the nondetection of a KN associated with GW190425 are still consistent with these parameters.

Figure 2 demonstrates how variations in sky coverage and $p_{\rm astro}$ can impact inferences in such a study in general. Our assumptions and derived constraints in this work correspond to ($p_{\rm astro} \sim 0.999$, sky coverage = 100%). However, as the sky coverage or astrophysical probability drops, the contribution of the survey upper limits to the posterior weakens and the constraints become broader. In particular, below a certain value for these parameters, the median apparent magnitudes inferred for the KNe are brighter than the median ZTF upper limits, pointing to the fact that at these values the alternative hypotheses—of either the KN being in a part of the sky where we do not have any observations or the KN event being a Terrestrial event—have more probability support. This result

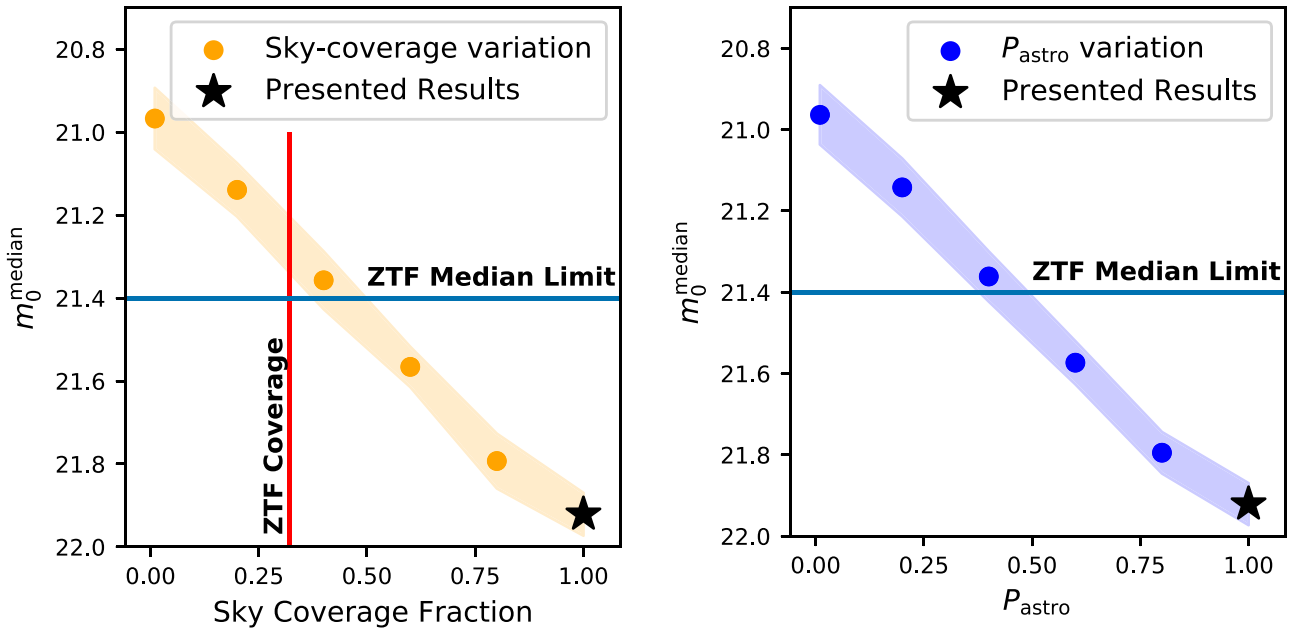

Figure 2. Variation in the median of the initial apparent magnitude distribution (assuming the source is at the mean luminosity distance from the 3D sky map) as a function of sky coverage (left) and probability of astrophysical origin $P_{\rm astro}$ (right). As the sky coverage/$P_{\rm astro}$ decreases (increases), constraints on the population parameter become weaker (stronger). Colored bands in both plots indicate the 2σ error regions from the interpolation of the posterior probabilities as mentioned in Section 3. Horizontal lines at $m = 21.4$ mag in both plots indicate the median limiting magnitude across the 3 day ZTF observations for GW190425. The red vertical line in the left plot indicates the actual sky coverage by ZTF.

also demonstrates the functionality of the framework to account for arbitrary values of these probabilistic factors that impact inference.

3.2. Comparison with `simsurvey`

In order to benchmark our results against those from complementary methods in the literature, we compare the limits we obtain via `nimbus` with those from the open-source simulator software `simsurvey`[20] (Feindt et al. 2019). `simsurvey` simulates KN detections (or injections) based on survey limits for any given event (Sagués Carracedo et al. 2021). We estimate the efficiency (or probability) of detecting a KN of a given initial absolute magnitude and linear evolution rate by comparing detections with the total injections within the observed fields. The software takes as input the ZTF pointings and information (i.e., the observation time, limiting magnitude, filters, and R.A. and decl. for each field and CCD) for the first three days after the merger and the 3D GW sky map for any given GW event. We simulate 100,000 KNe for a given absolute magnitude and evolution rate throughout the 3D GW probability region (see Figure 3). We assume a linear, colorless light-curve model as stated in Section 2.1. Our detection criteria require the KN to be detected at least once by ZTF: given actual detection experiments, this is a necessary but likely insufficient criterion for identification, because both color information and evolution rate are needed to separate KNe from false positives (Andreoni et al. 2020). For example, the gamma-ray burst afterglows that have been discovered in the past with the ZTF Realtime Search and Triggering (ZTFReST; Andreoni et al. 2021) pipeline have exhibited rapid evolution and reddening, requiring detections in both g and r bands, with $\geqslant$2 detections in either band for solid identification. Using `simsurvey` we account for Milky Way

[20] https://github.com/ZwickyTransientFacility/simsurvey

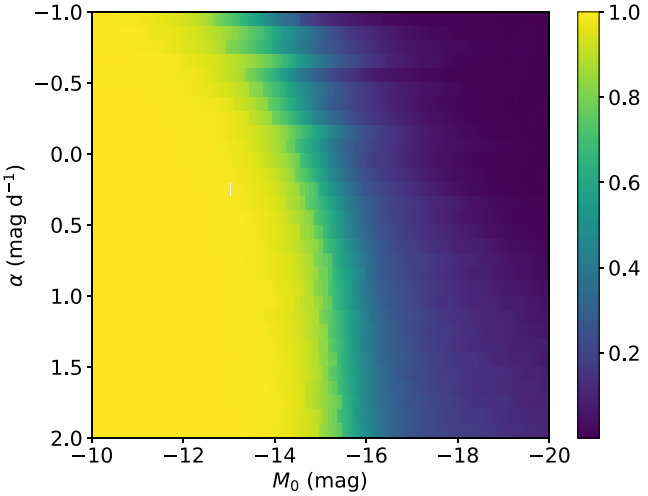

Figure 3. Nondetection probability $1 - \epsilon_i$, where ϵ_i is the recovery efficiency (number recovered/number injected) at a given absolute magnitude and evolution rate, for the grid of KNe simulated and recovered using `simsurvey`. We simulate 100,000 KNe in each bin, with magnitudes ranging from -10.0 to -20.0 mag and evolution rates ranging from -1.0 to 2.0 mag day^{-1}.

extinction and exclude any KNe with $E(B-V) > 2$ mag. This process is repeated for a range of magnitudes (100 bins between -10 and -20 mag) and evolution rates (31 bins from -1 and 2 mags per day) resulting in a grid of efficiencies. This grid of efficiencies is then converted into nondetection probabilities (see Figure 3).

As this is a nondetection study, `nimbus` generates posterior probabilities for models that are consistent with nondetection using observational upper limits; we compare the posterior support for models from `nimbus` with the detection efficiency estimates for the same models from `simsurvey`. We normalize the nondetection probabilities in the `simsurvey`

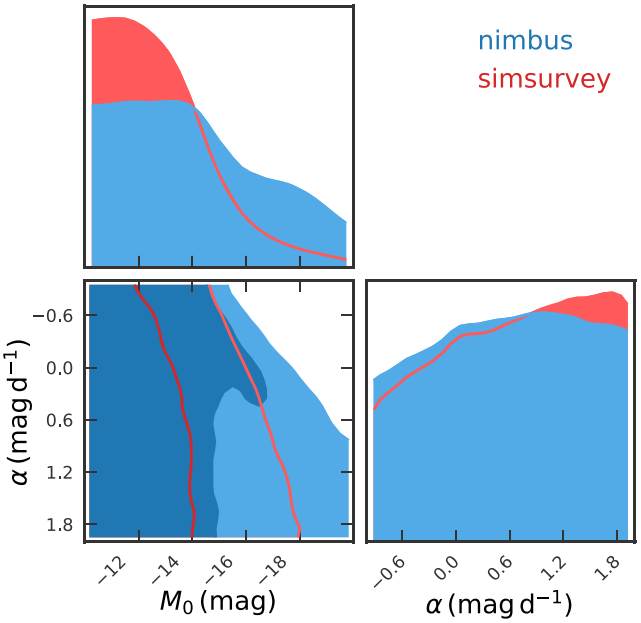

Figure 4. Comparison between `nimbus` and `simsurvey` with uniform priors. The corner plots compare the 2D and corresponding 1D marginalized posterior distributions for `nimbus` (blue) against the normalized nondetection probabilities from `simsurvey` (red). The 68% and 95% contours indicated on the plot demonstrate consistency between the two formalisms. We assume the same uniform priors in magnitude and evolution rate as in Figure 1.

model grid to sum to 1 in order to compare against `nimbus`. In Figure 4, we show the 2D and 1D marginalized posterior distributions for the two light-curve parameters from these formalisms.

We note that for `simsurvey`, the nondetection probability is calculated as $1.0 - \epsilon_i$, where ϵ_i is the recovery efficiency for a KN with a given absolute magnitude and evolution rate. Therefore, it naturally follows that as the initial absolute magnitude gets dimmer, our constraints get progressively worse. Likewise, going from rising to fast-fading KN models, the constraints become weaker.

In general, these comparisons illustrate consistency between the constraints inferred by the two methods on the brighter edge of the initial magnitude distribution, as evidenced by the 2D posterior in Figure 4. We observe a large overlap in the 1D marginalized posteriors for evolution rate for both formalisms. In both our hierarchical Bayesian formalism and the frequentist simulation-based approach, we observe that as the model evolution rate changes from -1.0 mag day^{-1} to $\sim$1.0 mag day^{-1}, constraints on KN models get progressively weaker. A rising KN is disfavored for values of M_0 on the brighter end of the initial magnitude range, as the transient would be brighter than these survey magnitudes. However, for evolution rates $>$1 mag day^{-1}, the effects of normalization in `nimbus` (see Section 2.3) take into account that the survey-limiting magnitudes lend more support to faster-decaying models, while the nightly limits themselves place nearly no constraints in this region of parameter space, leading to conservative estimates in the posterior curve relative to `simsurvey`. The 1D magnitude posteriors reveal that `nimbus` has broader support for KN models of varying absolute magnitudes (plateauing around $M \gtrsim -15$) and more conservative constraints compared to `simsurvey` for the brightest initial magnitudes.

Fundamentally, these two approaches are different but complementary. The `simsurvey` analysis yields the probability of not detecting a KN with (M_0, α) given the observations. `nimbus` gives the posterior probability for a KN with (M_0, α) that survives the upper limits. Thus, comparisons between these two approaches discussed here are analogous, but not exact. Note that while the results from `simsurvey` here might seem similar to those obtained in Figure 1 using the `mlim-distance` method of normalization, we emphasize that our preferred results using the `mlim-survey` method are more realistic in that they use the actual observed range of ZTF limiting magnitudes from the follow-up of GW190425. As stated before, the `mlim-distance` method uses the entire range of viable distances from the 3D GW sky map. One reason the `simsurvey` results could be similar to this method is that the `simsurvey` method also performs simulations in the entire region of the sky map based on the GW distance posterior. In order to better understand our results from the two formalisms, we also compared model probabilities using data from a single field of observation. Our results in this case show greater agreement, indicating that the differences in the main results arise from the fundamentally different treatment of combining multiple fields with varying upper limits, luminosity distance distributions, and different methods of model normalization.

3.3. Astrophysical Priors

Variations in the masses, velocities, composition of the ejecta, and inclination angle of the binary system result in different observed KN morphologies. BNS mass ejection mechanisms are categorized into two broad classes, i.e., dynamical ejecta and postmerger or wind ejecta (Nakar 2020). The tidal mass ejection occurring within $\sim$10 ms of the final inspiral stage is referred to as the dynamical ejecta. Bound NS material, which forms an accretion disk around the merger remnant, releases an outflow termed as the wind ejecta due to magnetically driven disk and neutrino winds.

Using priors inspired by realistic astrophysical models of KNe based on simulations, we present our Bayesian constraints with GW190425 in Figure 5. These priors are derived from surrogate models (Coughlin et al. 2018a) trained on the outputs of the Monte Carlo radiative-transfer code POSSIS (Bulla 2019). Previous studies have underscored the importance of using astrophysical light-curve priors in interpreting the emission from GW190425 (Barbieri et al. 2020; Foley et al. 2020; Kyutoku et al. 2020; Dudi et al. 2021; Nicholl et al. 2021; Raaijmakers et al. 2021). Broadly speaking, the surrogate models, otherwise referred to as phenomenological models, use a machine-learning technique to interpolate between data points. In this paper, we use a suite of 2D KN models assuming a three-component ejecta geometry, with dynamical ejecta split between equatorial lanthanide-rich and polar lanthanide-poor components, and a spherical disk-wind ejecta component at lower velocities and with compositions intermediate between lanthanide rich and lanthanide poor (Dietrich et al. 2020). The simulations cover four parameters: the inclination or the observer-viewing angle ($\theta_{\rm obs}$), dynamical ejecta mass ($M_{\rm dyn}$), postmerger or wind ejecta mass ($M_{\rm wind}$), and half-opening angle for the lanthanide-rich dynamical ejecta component (ϕ).

We assume a $\phi = 30^\circ$ half-opening angle and vary the other three parameters. Using the surrogate models, we predict BNS

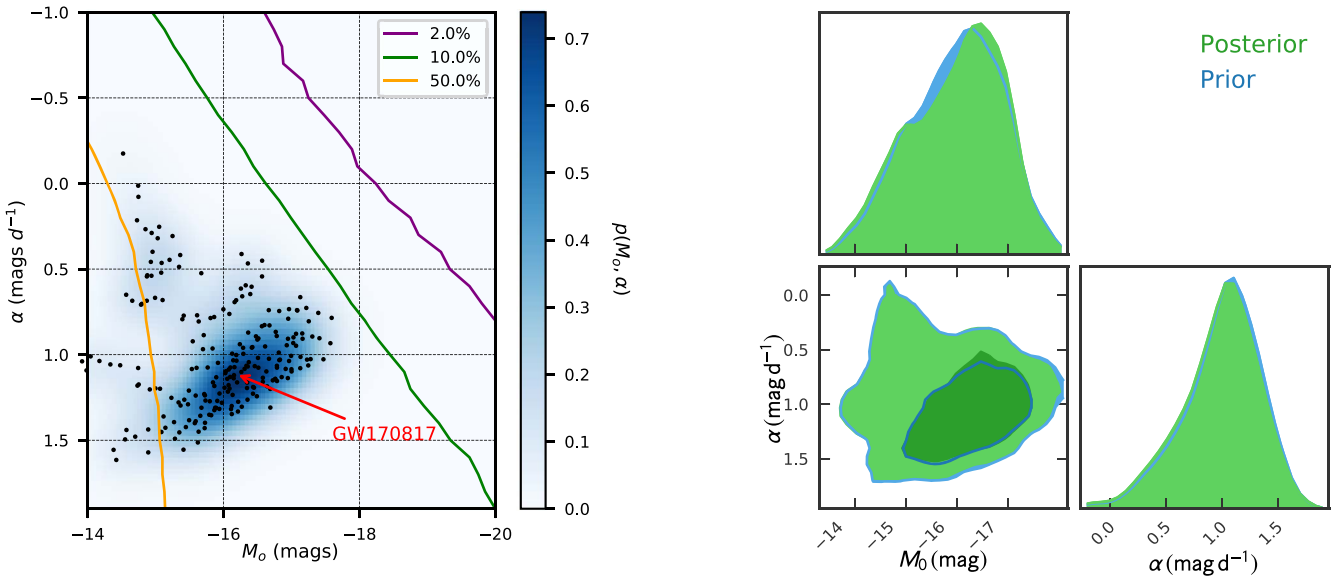

Figure 5. (Left) Bolometric priors, informed by radiative-transport-based KN models (Bulla 2019; Dietrich et al. 2020), showing regions of parameter space where particular luminosities and evolution rates are most probable or improbable for BNS KNe. To guide the eye, the best-fit model for GW170817 is highlighted. The nondetection percentiles (solid lines) are calculated using `simsurvey`, as discussed in Section 3.3. (Right) Corner plot showing the 2D and corresponding 1D marginalized posterior distributions (green) using model-based priors (blue). Contours indicate 68% and 95% confidence regions.

KN light curves for 10 viewing angles from a polar ($\theta_{\rm obs} = 0°$) to an equatorial ($\theta_{\rm obs} = 90°$) orientation, equally spaced in $\cos(\theta)$, and for the following ejecta masses: $M_{\rm dyn} \in [0.001, 0.005, 0.01, 0.02]$ and $M_{\rm wind} \in [0.01, 0.11]$ in steps of 0.02 $M_\odot$. In total, there are 240 BNS KN models. We then map from KN source properties (e.g., ejecta mass and inclination angle) to observables (peak magnitude and evolution rate) by performing light-curve fits.

A typical simulated BNS KN rapidly rises to a maximum within a day or two and gradually decays. Because the decaying period dominates, we fit a linear model from the entire grid's median phase of the peak magnitude up to 3 days since the merger for *g*-, *r*- and *i*-band KN light curves. We omitted 20 models that had a mean squared error greater than 0.1 from this process. These omitted models specifically had low $M_{\rm dyn}$ but high $M_{\rm wind}$. For each combination of source parameters, we then combine *g*-, *r*- and *i*-band peak magnitudes and evolution rates based on the number of simulated KNe in `simsurvey` that fall in the ZTF observed region of any specific filter. For GW190425, we have about 2614, 2930, and 168 out of 100,000 simulated KNe that fall in the region observed with *g*-, *r*- and *i*-band ZTF filters, respectively. Gathering the grid-based values for peak absolute magnitudes and decay rates of KNe, we use kernel density estimation to construct a smooth probability density function and approximate the true distribution for the models considered. The left panel of Figure 5 shows this grid-based prior model overlaid with the `simsurvey` nondetection probabilities.

Effectively, the astrophysical prior reduces a large portion of the parameter space previously considered by the uniform prior choice. The 2%, 10%, and 50% nondetection percentiles estimated using `simsurvey` are plotted over the astrophysical priors. Though the probable prior region is mostly encompassed by the 50% curve, it lies entirely to the left of the 2% and 10% curves, indicating that our GW190425 ZTF observations are not deep enough to place stringent constraints over the astrophysical priors. This is reflected in the inference results from `nimbus` (right panel of Figure 5) based on the astrophysical prior assumptions. Specifically, the posterior and prior contour lines overlap considerably, showing that almost all of the KN models supported by the astrophysical prior survive the upper limits. In general, this implementation demonstrates the ability to use theory and simulation-based astrophysical models within the `nimbus` framework and constrain them.

4. Discussion and Future Outlook

In this paper, we have presented a hierarchical Bayesian framework `nimbus` that leverages data from nondetections of probable KNe. This Python package utilizes GW and EM follow-up information from each candidate event to provide posterior distributions for KN model parameters. The framework also accounts for the probability of an event being astrophysical. Although the analysis presented here focuses on a single BNS event, GW190425, the framework has the capability to include multiple events. It is also straightforward to extend the framework to model the inference based on subpopulations of KN candidates such as BNS and NSBH mergers. We hope the multimessenger astrophysics community finds use for and benefits from this package.

A current limitation of this study is that the framework does not account for events that have been detected in EM follow-up. In order to place stringent constraints on KN parameters, it would be ideal to include potential candidates for which there exist data from detected light curves. However, including information from detected events into the framework would involve nontrivial changes to the model likelihood and would necessitate an accurate understanding of survey selection effects. So far, GW170817 (Abbott et al. 2017a) is the only GW event to have been associated with a KN counterpart (Abbott et al. 2017b). Numerous studies in the literature (e.g., Cowperthwaite et al. 2017; Drout et al. 2017; Arcavi 2018; Andreoni et al. 2020) have extrapolated follow-up data to arrive at an estimate of its initial absolute magnitude and decay

rate. In particular, Kasliwal et al. (2020) compared their results to an extrapolated initial magnitude of −16.6 mag with a decay rate of 1 mag per day. Our results do indicate nonnegligible posterior support for such a model. Nevertheless, this represents a single point in model parameter space, and we would instead require a number of detected events to inform the population of KNe. Further, restricting the study to nondetections is motivated by the fact that O3 did not yield any obvious EM counterparts. We defer the development of including detected events to a future study.

We presented the results of our inference on GW190425 using two different prior choices for our model parameters (see Figures 1 and 5). Our first choice, which is uniform in the parameters, is representative of an inference that is carried out with uninformative assumptions. Our second prior choice is based on surrogate models from Monte Carlo radiative-transfer simulations of KNe (Coughlin et al. 2018a; Bulla 2019) and takes into account the effect of variations in ejecta masses and inclination angle on the resulting KN morphology. The inference using such a prior represents the possibility of testing realistic, physical models of KNe against upper limits obtained from surveys. While our implementation with uniform priors constrained the prior parameter space to a considerable extent and shows consistency with previous efforts (Kasliwal et al. 2020), the posterior results based on surrogate KN models are largely uninformative with respect to the prior. Overall, these results show how priors on model parameters can influence the constraints obtained and the need to examine results in light of the prior distribution.

One of the assumptions we have made in presenting our results above is that the KN counterpart to GW190425 is localized within the surveyed region of the sky map. GW190425, as mentioned previously in Section 3, had an overall sky coverage by ZTF of ∼32%. Given that a significant fraction of the sky map is not surveyed and therefore would result in uninformative constraints, we made this assumption to demonstrate the utility of the Bayesian framework. In LIGO–Virgo–KAGRA's fourth observing run, we expect that for ∼8%–10% of BNS and NSBH systems discovered, ZTF will be able to observe >90% of the localization (Petrov et al. 2022), and hence our above assumption would hold reasonably true in those particular cases.

Furthermore, throughout this study we have assumed a KN luminosity evolution model that is linear in time. A linear model only needs two parameters to define it, and our goal in this paper has been to demonstrate framework functionality at the cost of model accuracy. Such a simplistic choice might not be representative of realistic evolution models (see Metzger 2019) that depend on more complex parameters related to the binary system. In principle, it should be feasible to include arbitrary models for luminosity evolution because the framework only expects a function that returns predictions for the absolute magnitude of the KN as a function of time. For all priors applied, we consider only the first three days of evolution of the KN (and therefore the first three days of observations after the merger time of GW190425). This choice is motivated by the fact that ZTF is unlikely to detect a KN at the distance of GW190425 in the g and r bands 3 days postmerger. More specifically, at 4 days, all KN models in our set have an apparent magnitude in the g and r bands fainter than the median depth of ZTF in this study (∼21 mag).

In this work we also ignored color evolution in our studies of KN nondetections. In addition to differentiating observations in different filters, in the future we intend to account for the K-correction effect on KN color evolution, which is especially relevant for cosmological sources. We will implement this feature in `nimbus` following the existing implementation in `simsurvey`.

We highlight here that due to the adaptability of `nimbus` to various light-curve models and a hierarchical framework, it could even be used to jointly constrain the properties of a potential KN and short gamma-ray burst optical afterglow associated with the GW event (as in Dietrich et al. 2020; P. T. H. Pang et al., in preparation) based on the rapid optical follow-up performed by various facilities.

In order to establish consistency with existing results in the literature, we compared our results to those from the simulator software `simsurvey`. As shown in Figure 4, the two formalisms are largely consistent, although some qualitative differences exist. In the future, with observations and upper limits from more events, it will be possible to test for further consistency between frameworks investigating KN populations.

In our specific implementation with astrophysical priors in Section 3.1, we used a prior on the KN luminosity parameters, i.e., the initial absolute magnitude and evolution rate that depends on intrinsic parameters such as the dynamical or wind ejecta masses. Our Bayesian approach makes it straightforward to convert our posteriors on the luminosity parameters into constraints on these intrinsic parameters. Alternatively, because the framework is agnostic to the KN model used, it should be possible to directly use priors on the physical parameters that govern the light-curve morphology. In such a case, the inference would directly constrain parameters such as the ejecta mass from the binary merger, although the computational feasibility of such an implementation needs to be investigated. The use of these astrophysical priors is based on including variations in the observer-viewing (inclination) angle and its effect on each KN model. Nontrivial couplings between the observer angle and the signal-to-noise ratio of the GW signal can lead to some selection bias. To mitigate this effect in the future, we will select sky maps from a realistic distribution of GW signals detected by LIGO (Petrov et al. 2022), which will inform the distribution of observer angles for our KN models.

Looking forward to O4 and beyond, we expect that `nimbus` will be an important framework for analyzing joint EM–GW observations. Petrov et al. (2022) predict a median of ∼35 BNS yr^{-1} with O4 sensitivity and roughly double the number during O5. Thus, with several tens of EM follow-ups of BNS events from O4 and O5, we will use `nimbus` to place stringent population-level luminosity function constraints based on nondetections. For the well-localized ($\lesssim$100 deg^2) and nearby ($\lesssim$200 Mpc) events (predicted to range from 0–13 BNS mergers; Petrov et al. 2022) detected by LIGO in O4 for which we have excellent optical sky coverage, `nimbus` is ideally placed to constrain the intrinsic KN properties, which can translate to constraints on binary system parameters such as mass ratio and NS radius in the face of nondetection. A similar analysis of NSBH mergers is also feasible, though ejecta mass yield sensitively depends on the mass ratio of the system (e.g., Krüger & Foucart 2020). As a follow-up study, we hope to explore the scientific merit of conducting EM–GW follow-ups with the Vera C. Rubin Observatory, assuming the cadence and

filter strategy for KN identification outlined in Andreoni et al. (2021), using the `nimbus` framework.

Constraining the ejecta masses of the KN population could potentially provide us better insights into the amount of *r*-process material contributed to the formation of KNe (Hotokezaka et al. 2018). It will also help in understanding the relationship and breaking the degeneracy that exists between binary parameters (equation of state, spin, and mass ratio) (Foucart et al. 2018; Hinderer et al. 2019; Radice & Dai 2019; Zhu et al. 2021a), ejecta mass, and KN light-curve morphology. (Coughlin et al. 2019a; Hotokezaka & Nakar 2020; Breschi et al. 2021; Raaijmakers et al. 2021). The future GW and EM multimessenger landscape will provide the opportunity to explore this further.

Based on observations obtained with the Samuel Oschin Telescope 48 inch and the 60 inch Telescope at the Palomar Observatory as part of the Zwicky Transient Facility project. ZTF is supported by the National Science Foundation under grant No. AST-1440341 and a collaboration including Caltech, IPAC, the Weizmann Institute for Science, the Oskar Klein Center at Stockholm University, the University of Maryland, the University of Washington, Deutsches Elektronen-Synchrotron and Humboldt University, Los Alamos National Laboratories, the TANGO Consortium of Taiwan, the University of Wisconsin at Milwaukee, and Lawrence Berkeley National Laboratories. Operations are conducted by COO, IPAC, and UW. This work was supported by the GROWTH (Global Relay of Observatories Watching Transients Happen) project funded by the National Science Foundation under PIRE grant No. 1545949. GROWTH is a collaborative project among the California Institute of Technology (USA), University of Maryland College Park (USA), University of Wisconsin-Milwaukee (USA), Texas Tech University (USA), San Diego State University (USA), University of Washington (USA), Los Alamos National Laboratory (USA), Tokyo Institute of Technology (Japan), National Central University (Taiwan), Indian Institute of Astrophysics (India), Indian Institute of Technology Bombay (India), Weizmann Institute of Science (Israel), The Oskar Klein Centre at Stockholm University (Sweden), Humboldt University (Germany), Liverpool John Moores University (UK), and University of Sydney (Australia). S.R.M. thanks the LSSTC Data Science Fellowship Program, which is funded by LSSTC, NSF Cybertraining Grant #1829740, the Brinson Foundation, and the Moore Foundation; his participation in the program has benefited this work. S. R.M. and J.C. acknowledge support from the NSF grant NSF PHY #1912649. We are grateful for the computational resources provided by the Leonard E Parker Center for Gravitation, Cosmology and Astrophysics at the University of Wisconsin-Milwaukee. M.M.K. acknowledges generous support from the David and Lucille Packard Foundation. M. C. and M.S. acknowledge support from the National Science Foundation with grant number PHY-2010970. S.A. acknowledges support from the GROWTH PIRE grant No. 1545949. A. S.C acknowledges support from the G.R.E.A.T research environment, funded by *Vetenskapsrådet*, the Swedish Research Council, project number 2016-06012. M.B. acknowledges support from the Swedish Research Council (Reg. no. 2020-03330). We thank the reviewer whose comments and suggestions helped improve and clarify this manuscript.

Facilities: LIGO, ZTF/PO:1.2m.

Software: `ipython` (Pérez & Granger 2007), `jupyter` (Kluyver et al. 2016), `matplotlib` (Hunter 2007), `python` (Van Rossum & Drake 2009), `NumPy` (Harris et al. 2020), `scikit-learn` (Pedregosa et al. 2011), `scipy` (Virtanen et al. 2020).

ORCID iDs

Siddharth R. Mohite https://orcid.org/0000-0003-1356-7156
Shreya Anand https://orcid.org/0000-0003-3768-7515
David L. Kaplan https://orcid.org/0000-0001-6295-2881
Michael W. Coughlin https://orcid.org/0000-0002-8262-2924
Jolien Creighton https://orcid.org/0000-0003-3600-2406
Patrick R. Brady https://orcid.org/0000-0002-4611-9387
Tomás Ahumada https://orcid.org/0000-0002-2184-6430
Igor Andreoni https://orcid.org/0000-0002-8977-1498
Mattia Bulla https://orcid.org/0000-0002-8255-5127
Matthew J. Graham https://orcid.org/0000-0002-3168-0139
Mansi M. Kasliwal https://orcid.org/0000-0002-5619-4938
Russ R. Laher https://orcid.org/0000-0003-2451-5482
Kyung Min Shin https://orcid.org/0000-0002-1486-3582
David L. Shupe https://orcid.org/0000-0003-4401-0430
Leo P. Singer https://orcid.org/0000-0001-9898-5597

References

Aasi, J., Abbott, B. P., Abbott, R., et al. 2015, CQGra, 32, 074001
Abbott, B. P., Abbott, R., Abbott, T. D., et al. 2017a, PhRvL, 119, 161101
Abbott, B. P., Abbott, R., Abbott, T. D., et al. 2017b, ApJL, 848, L12
Abbott, B. P., Abbott, R., Abbott, T. D., et al. 2017c, ApJL, 850, L39
Abbott, B. P., Abbott, R., Abbott, T. D., et al. 2019, PhRvX, 9, 031040
Abbott, B. P., Abbott, R., Abbott, T. D., et al. 2020, ApJL, 892, L3
Abbott, R., Abbott, T. D., Abraham, S., et al. 2021, PhRvX, 11, 021053
Acernese, F., Agathos, M., Agatsuma, K., et al. 2015, CQGra, 32, 024001
Anand, S., Coughlin, M. W., Kasliwal, M. M., et al. 2020, NatAs, 5, 46
Andreoni, I., Ackley, K., Cooke, J., et al. 2017, PASA, 34, e069
Andreoni, I., Coughlin, M. W., Kool, E. C., et al. 2021, ApJ, 918, 63
Andreoni, I., Goldstein, D., Kasliwal, M. M., et al. 2020, ApJ, 890, 131
Andreoni, I., Margutti, R., Sharan Salafia, O., et al. 2021, arXiv:2111.01945
Antier, S., Agayeva, S., AlMualla, M., et al. 2020, MNRAS, 497, 5518
Arcavi, I. 2018, ApJL, 855, L23
Barbieri, C., Salafia, O. S., Colpi, M., Ghirlanda, G., & Perego, A. 2020, A&A, 654, A12
Barnes, J., Kasen, D., Wu, M.-R., & Martínez-Pinedo, G. 2016, ApJ, 829, 110
Barnes, J., Zhu, Y. L., Lund, K. A., et al. 2021, ApJ, 918, 44
Bauswein, A., Baumgarte, T. W., & Janka, H.-T. 2013, PhRvL, 111, 131101
Bellm, E. C., Kulkarni, S. R., Graham, M. J., et al. 2019, PASP, 131, 018002
Blazek, M., Christensen, N., Howell, E., et al. 2019, GCN, 24227, 1
Breschi, M., Perego, A., Bernuzzi, S., et al. 2021, MNRAS, 505, 1661
Bulla, M. 2019, MNRAS, 489, 5037
Chambers, K. C., Magnier, E. A., Metcalfe, N., et al. 2016, arXiv:1612.05560
Chornock, R., Berger, E., Kasen, D., et al. 2017, ApJL, 848, L19
Côté, B., Fryer, C. L., Belczynski, K., et al. 2018, ApJ, 855, 99
Coughlin, M. W., Ahumada, T., Anand, S., et al. 2019c, ApJL, 885, L19
Coughlin, M. W., Ahumada, T., Cenko, S. B., et al. 2019d, PASP, 131, 048001
Coughlin, M. W., Dietrich, T., Antier, S., et al. 2019b, MNRAS, 492, 863
Coughlin, M. W., Dietrich, T., Doctor, Z., et al. 2018a, MNRAS, 480, 3871
Coughlin, M. W., Dietrich, T., Margalit, B., & Metzger, B. D. 2019a, MNRAS, 489, L91
Coughlin, M. W., Tao, D., Chan, M. L., et al. 2018b, MNRAS, 478, 692
Coulter, D. A., Foley, R. J., Kilpatrick, C. D., et al. 2017, Sci, 358, 1556
Cowperthwaite, P. S., Berger, E., Villar, V. A., et al. 2017, ApJL, 848, L17
De, K., Adams, S. M., Coughlin, M., et al. 2019, GCN, 24187, 1
de Jaeger, T., Shappee, B. J., Kochanek, C. S., et al. 2022, MNRAS, 509, 3427
Dekany, R., Smith, R. M., Riddle, R., et al. 2020, PASP, 132, 038001
Dhawan, S., Bulla, M., Goobar, A., Sagués Carracedo, A., & Setzer, C. N. 2020, ApJ, 888, 67
Dietrich, T., Coughlin, M. W., Pang, P. T. H., et al. 2020, Sci, 370, 1450
Drout, M. R., Piro, A. L., Shappee, B. J., et al. 2017, Sci, 358, 1570

Dudi, R., Adhikari, A., Brügmann, B., et al. 2021, arXiv:2109.04063
Etienne, Z. B., Liu, Y. T., Shapiro, S. L., & Baumgarte, T. W. 2009, PhRvD, 79, 044024
Evans, P. A., Cenko, S. B., Kennea, J. A., et al. 2017, Sci, 358, 1565
Farr, W. M., Gair, J. R., Mandel, I., & Cutler, C. 2015, PhRvD, 91, 023005
Feindt, U., Nordin, J., Rigault, M., et al. 2019, JCAP, 2019, 005
Foley, R. J., Coulter, D. A., Kilpatrick, C. D., et al. 2020, MNRAS, 494, 190
Foucart, F., Hinderer, T., & Nissanke, S. 2018, PhRvD, 98, 081501
Foucart, F., Moesta, P., Ramirez, T., et al. 2021, PhRvD, 104, 123010
Gaebel, S. M., Veitch, J., Dent, T., & Farr, W. M. 2019, MNRAS, 484, 4008
Ghosh, S., Chatterjee, D., Kaplan, D. L., Brady, P. R., & Sistine, A. V. 2017, PASP, 129, 114503
Gompertz, B., Cutter, R., Steeghs, D., et al. 2020, MNRAS, 497, 726
Górski, K. M., Hivon, E., Banday, A. J., et al. 2005, ApJ, 622, 759
Graham, M. J., Kulkarni, S. R., Bellm, E. C., et al. 2019, PASP, 131, 078001
Green, G. 2018, JOSS, 3, 695
Harris, C. R., Millman, K. J., van der Walt, S. J., et al. 2020, Natur, 585, 357
Heinzel, J., Coughlin, M. W., Dietrich, T., et al. 2021, MNRAS, 502, 3057
Hinderer, T., Nissanke, S., Foucart, F., et al. 2019, PhRvD, 100, 063021
Hosseinzadeh, G., Cowperthwaite, P. S., Gomez, S., et al. 2019, ApJL, 880, L4
Hotokezaka, K., Beniamini, P., & Piran, T. 2018, IJMPD, 27, 1842005
Hotokezaka, K., Kiuchi, K., Kyutoku, K., et al. 2013, PhRvD, 87, 024001
Hotokezaka, K., & Nakar, E. 2020, ApJ, 891, 152
Hotokezaka, K., Nakar, E., Gottlieb, O., et al. 2019, NatAs, 3, 940
Hunter, J. D. 2007, CSE, 9, 90
Just, O., Kullmann, I., Goriely, S., et al. 2022, MNRAS, 510, 2820
Kasen, D., Fernández, R., & Metzger, B. D. 2015, MNRAS, 450, 1777
Kasen, D., Metzger, B., Barnes, J., Quataert, E., & Ramirez-Ruiz, E. 2017, Natur, 551, 80
Kasliwal, M. M. 2011, PhD thesis, California Institute of Technology
Kasliwal, M. M., Anand, S., Ahumada, T., et al. 2020, ApJ, 905, 145
Kasliwal, M. M., Coughlin, M. W., Bellm, E. C., et al. 2019, GCN, 24191, 1
Kasliwal, M. M., Kasen, D., Lau, R. M., et al. 2022, MNRAS, 510, L7
Kasliwal, M. M., Nakar, E., Singer, L. P., et al. 2017, Sci, 358, 1559
Kawaguchi, K., Kyutoku, K., Shibata, M., & Tanaka, M. 2016, ApJ, 825, 52
Kawaguchi, K., Shibata, M., & Tanaka, M. 2020, ApJ, 889, 171
Kilpatrick, C. D., Foley, R. J., Kasen, D., et al. 2017, Sci, 358, 1583
Kiuchi, K., Kyutoku, K., Shibata, M., & Taniguchi, K. 2019, ApJL, 876, L31
Kluyver, T., Ragan-Kelley, B., Pérez, F., et al. 2016, in Positioning and Power in Academic Publishing: Players, Agents and Agendas, ed. F. Loizides & B. Scmidt (Netherlands: IOS Press), 87
Köppel, S., Bovard, L., & Rezzolla, L. 2019, ApJL, 872, L16
Korobkin, O., Wollaeger, R., Fryer, C., et al. 2021, ApJ, 910, 116
Krüger, C. J., & Foucart, F. 2020, PhRvD, 101, 103002
Kullmann, I., Goriely, S., Just, O., et al. 2022, MNRAS, 510, 2804
Kyutoku, K., Fujibayashi, S., Hayashi, K., et al. 2020, ApJL, 890, L4
Kyutoku, K., Ioka, K., Okawa, H., Shibata, M., & Taniguchi, K. 2015, PhRvD, 92, 044028
Levan, A. 2020, in The New Era of Multi-Messenger Astrophysics (ASTERICS 2019) (Trieste: PoS), 044
Li, B., Xu, D., Zhou, X., & Lu, H. 2019, GCN, 24285, 1
Li, L.-X., & Paczyński, B. 1998, ApJL, 507, L59
Lipunov, V., Gorbovskoy, E., Kornilov, V., et al. 2019, GCN, 24167, 1
Lipunov, V. M., Gorbovskoy, E., Kornilov, V. G., et al. 2017, ApJL, 850, L1
Lundquist, M. J., Paterson, K., Fong, W., et al. 2019a, ApJL, 881, L26
Lundquist, M. J., Paterson, K., Sand, D. J., et al. 2019b, GCN, 24172, 1
Mandel, I., Farr, W. M., & Gair, J. R. 2019, MNRAS, 486, 1086
Masci, F. J., Laher, R. R., Rusholme, B., et al. 2019, PASP, 131, 018003
McBrien, O., Smartt, S., Smith, K. W., et al. 2019, GCN, 24197, 1
McCully, C., Hiramatsu, D., Howell, D. A., et al. 2017, ApJL, 848, L32
Metzger, B. D. 2019, LRR, 23, 1
Metzger, B. D., Martínez-Pinedo, G., Darbha, S., et al. 2010, MNRAS, 406, 2650
Mohite, S. R. 2021, nimbus : A Bayesian inference framework to constrain kilonova models., v1.0.0, Zenodo, doi:10.5281/zenodo.5648468
Morgan, R., Soares-Santos, M., Annis, J., et al. 2020, ApJ, 901, 83
Nakar, E. 2020, PhR, 886, 1
Nicholl, M., Berger, E., Kasen, D., et al. 2017, ApJL, 848, L18
Nicholl, M., Margalit, B., Schmidt, P., et al. 2021, MNRAS, 505, 3016
Pedregosa, F., Varoquaux, G., Gramfort, A., et al. 2011, JMLR, 12, 2825
Perego, A., Radice, D., & Bernuzzi, S. 2017, ApJL, 850, L37
Pérez, F., & Granger, B. E. 2007, CSE, 9, 21
Petrov, P., Singer, L. P., Coughlin, M. W., et al. 2022, ApJ, 924, 54
Pian, E., D'Avanzo, P., Benetti, S., et al. 2017, Natur, 551, 67
Raaijmakers, G., Nissanke, S., Foucart, F., et al. 2021, ApJ, 922, 269
Radice, D., & Dai, L. 2019, EPJA, 55, 50
Radice, D., Perego, A., Hotokezaka, K., et al. 2018, ApJ, 869, 130
Roberts, L. F., Kasen, D., Lee, W. H., & Ramirez-Ruiz, E. 2011, ApJL, 736, L21
Rosswog, S. 2005, ApJ, 634, 1202
Rosswog, S., Feindt, U., Korobkin, O., et al. 2017, CQGra, 34, 104001
Sagués Carracedo, A., Bulla, M., Feindt, U., & Goobar, A. 2021, MNRAS, 504, 1294
Sasada, M., Utsumi, Y., Itoh, R., et al. 2021, PTEP, 2021, 05A104
Schlafly, E. F., & Finkbeiner, D. P. 2011, ApJ, 737, 103
Shappee, B. J., Simon, J. D., Drout, M. R., et al. 2017, Sci, 358, 1574
Siegel, D. M. 2019, EPJA, 55, 203
Singer, L. P., Chen, H.-Y., Holz, D. E., et al. 2016a, ApJL, 829, L15
Singer, L. P., Chen, H.-Y., Holz, D. E., et al. 2016b, ApJS, 226, 10
Singer, L. P., & Price, L. R. 2016, PhRvD, 93, 024013
Smartt, S. J., Chen, T. W., Jerkstrand, A., et al. 2017, Natur, 551, 75
Smith, K., Young, D., McBrien, O., et al. 2019, GCN, 24210, 1
Soares-Santos, M., Holz, D., Annis, J., Chornock, R., & Herner, K. 2017, ApJL, 848, L16
Steeghs, D., Dyer, M., Galloway, D., et al. 2019, GCN, 24224, 1
Tanaka, M. 2016, AdAst, 2016, 634197
Tanaka, M., & Hotokezaka, K. 2013, ApJ, 775, 113
Tanaka, M., Kato, D., Gaigalas, G., et al. 2018, ApJ, 852, 109
Tanaka, M., Utsumi, Y., Mazzali, P. A., et al. 2017, PASJ, 69, 102
Tanvir, N. R., Levan, A. J., González-Fernández, C., et al. 2017, ApJL, 848, L27
Tonry, J. L., Denneau, L., Heinze, A. N., et al. 2018, PASP, 130, 064505
Utsumi, Y., Tanaka, M., Tominaga, N., et al. 2017, PASJ, 69, 101
Van Rossum, G., & Drake, F. L. 2009, Python 3 Reference Manual (Scotts Valley, CA: CreateSpace)
Veitch, J., Raymond, V., Farr, B., et al. 2015, PhRvD, 91, 042003
Virtanen, P., Gommers, R., Oliphant, T. E., et al. 2020, NatMe, 17, 261
Waxman, E., Ofek, E. O., Kushnir, D., & Gal-Yam, A. 2018, MNRAS, 481, 3423
Wollaeger, R. T., Korobkin, O., Fontes, C. J., et al. 2018, MNRAS, 478, 3298
Wu, M.-R., Barnes, J., Martínez-Pinedo, G., & Metzger, B. D. 2019, PhRvL, 122, 062701
Xu, D., Zhu, Z. P., Yu, B. Y., et al. 2019, GCN, 24190, 1
Zhu, J.-P., Wu, S., Yang, Y.-P., et al. 2021a, ApJ, 917, 24
Zhu, J.-P., Yang, Y.-P., Zhang, B., Gao, H., & Yu, Y.-W. 2021b, arXiv:2110.10468
Zhu, Y., Wollaeger, R. T., Vassh, N., et al. 2018, ApJL, 863, L23